Investigation on the Modeling and Simulation of Hydrodynamics in Asymmetric Laser Micro-Welding of Austenitic Stainless Steel and its Process Optimization

José Luis Velázquez de la Hoz[1] and Kai Cheng[1]

[1] *College of Engineering, Design and Physical Sciences, Brunel University London, Uxbridge UB8 3PH, UK*

ABSTRACT

Laser micro-welding is a joining technology utilized across various high-value industries, like medical, automotive, e-mobility, and aerospace. A trial-and-error process to identify welding parameters does not necessarily lead to optimized quality levels. Furthermore, offline non-destructive examination methods often launched to verify welding quality may inadvertently trigger excessive costs and time delays, ultimately failing to guarantee defect-free welds. In response to these challenges, this article introduces an advanced multiscale model designed to unravel the intricate dynamics of hydrodynamics and the overarching physics within laser micro-welding melting pools. Developed using the COMSOL software package, the model adeptly demonstrates how surface tension gradients shape the geometry of welds, thus influencing their quality. This knowledge allows the mapping of welding defects. One of the novelties of the article is to introduce geometric dissimilar welding conditions by simulating an asymmetric edge joint. It shows a study on a new, unstudied way to laser weld with many applications in the field. The model further establishes its utility in design experiments to determine parameter, tolerance, and system design. Moreover, the insights garnered from understanding and controlling these drivers have far-reaching implications for the advancement of subsequent methodological research and the development of in-situ

quality control practices by mapping the welding defects. Finally, the article shows that the discouraging high computational costs restrict its potential application to support a Digital Twin.

1. Introduction

Strictly speaking, a micro-weld displays dimensional attributes, like length, width, or depth, below one mm.[1] Laser micro-welding is a specific joining technology supporting a host of high-value manufacturing industries, including medical, microelectronics, automotive, e-mobility, and aerospace. The melting front hydrodynamics has a fundamental impact on welding geometry.[2,3] A weldment's geometry assumes a pivotal role in welding quality, as it not only imparts mechanical attributes, such as mechanical strength, fatigue resistance, and corrosion resistance, but also significantly influences microstructure through temperature gradients and cooling rates.[4] The joint configuration, in turn, shapes the cooling rate due to the inherent irregular heat distribution. Typically prescribed at the product design phase, in practical terms, however, attaining a specific weld morphology imposes some challenges due to the inevitable presence of manufacturing variability, the small sizes involved, the short processing times, and the customized or personalized pressures from the demand side.[5]

Substantial non-linearities, typically characterizing the micro molten metal pools, are very responsive to boundary conditions.[6] Supplementary variability sources that magnify the process complexity are new batch chemistry differences, tooling wear-out, or operators' influence in part setting.[7] More governable but equipment-dependent factors that shape the weld's geometry are the spatial and temporal distribution of laser energy on the surface of the workpiece, like power density or processing time.[8] Moreover, small

batches of large product varieties, often encountered in micro-welded product customization, impede profiting from the benefits of the economy of scales, in which long production series typically allow the progressive fine-tuning of welding parameters. Widely used hands-on trial-and-error processes to identify welding process parameters cannot suffice to manage this complexity.[9] Advanced multiscale simulation and modeling techniques can significantly aid this pursuit by providing an enhanced understanding of the physical phenomena in micro-laser welding hydrodynamics.

Micro laser welding has two regimes: keyhole and conduction laser micro welding. Keyhole laser emerges when power densities beyond $1\,MW/cm^2$ are applied.[10] High depth-to-width ratios characterize its geometries. Localized heat concentration prompts material evaporation due to temperatures surpassing the boiling point.[11] This bounded boiling material forms a cylinder of vaporized material, or keyhole, that moves along the power source's path. High processing power and high scanning speed regimes determine the hydrodynamic complexity. Keyhole laser welding involves five distinctive flow drivers, namely surface tension, thermocapillarity, recoil pressure, buoyancy, and material evaporation.[12]

Examples of advanced multiscale simulation for keyhole laser micro welding exist. Schöler et al., for instance, proposed a model to simulate a copper keyhole micro-welding process at high power (between 850 and 1500W continuous wave) and high speeds (between 80 and 10 mm·s^{-1}). Capillary forces were balanced out by recoil pressure and surface forces were removed from the analysis.[13] Patel and his coworker simulated a CW lap joint laser micro weld of 100 µm, stainless steel AISI304 thin sheets.[14] They used a 100W continuous wave and a scanning speed of 300 mm·s^{-1}, which causes a deep and narrow weld that eliminates the free surface from the analysis. An emerging keyhole reaching both plates was simulated successfully. In another study, Wu et al.[15] in an experiment and its corresponding simulation using 0.8 mm plates of AISI 304L and pure grade 2 titanium, TA2, and continuous wave laser power between 500 and 520 W and traveling speeds 3.2 and 3.6 m/min^{-1} confirms that the recoil pressure forms keyholes, where walls are used for heat distribution and fluid flow and diffusion are responsible for mass transfer.

Although much scarcer, modeling and simulation conduction laser micro welding under symmetric melting conditions has also received attention in the literature. It occurs when power densities are below 0.5 MW/cm^2 [16] greatly reducing the weldment's aspect ratio. While typically negligible for more sizable welds, capillarity and thermocapillarity are essential to characterize the flow of these melting micropools.[17] Laser processing generates significant interfacial temperature differences that provoke surface tension gradients over the surface of the melting pool. Without surfactants, these gradients drive the metal outwardly tangential. The laser Gaussian intensity distribution promotes these sharp temperature and surface tension gradients. Capillarity generates a bulge in the pool that competes with thermocapillarity.

While still intricate, high-speed conduction laser micro welding permits mathematical simplifications by enabling the use of a more manageable flat weld surface model. Thus, in another work, Patel and his team[18] devised a high-speed simulation model for conduction-mode, micro-laser welding that could characterize the behavior of the pool in terms of velocity and temperature. The flat surface assumption helped discard the effects of capillarity from the model. The available literature also examines surfactant concentration gradients. Sharma et al. analyzed the effects of chemo-capillarity, a widely reported phenomenon by which the substantial presence of surfactants on the surface, like sulfur, can counteract and even reverse the effects of thermocapillarity.

The present study addresses low-power, low-speed conduction microscale welding, an area of welding research that has received relatively little attention. Laser melting processing, as it is commonly known, is at the core of a wide array of applications, including micro-drilling, micro-welding, micro-cutting , micro-texturing, micro-polishing additive manufacturing, and micro welding that allow interchange analysis with little to no modification.[6,19–22] Next to their conduction regime, these processes share defining characteristics like lower power, and traveling speeds. The melting pool is shallower. There is no keyhole as temperatures are below boiling point. A hotter, free surface forms, which causes larger temperature gradients and, thus, higher thermocapillary forces[4], the flow drivers. Then, a necessity for employing the

free surface assumption emerges when describing the interface between molten metal and shielding gas, resulting in an increased level of modeling complexity. Common to all, a diminutive Reynolds number for the melting pool implies the role of viscous forces relative to inertial forces is significantly amplified, suggesting slow hydrodynamics fronts. In this context, surface tension-induced forces are inertial. Ultimately, the debate circles around the individual effect and alternating dominance of either one of these two drivers in the melting pool hydrodynamics: thermocapillarity and capillarity to understand and manage it.

In the laser micro melting realm, Yang et al. built a model according to the surface morphology forming mechanism. They attempted to understand the influence of capillarity force and thermocapillary force on the flow forming in laser micro melting surface morphology. They added, however, a very important variable, the recoil pressure which would be responsible for the oscillation of the molten pool surface. Their result shows that recoil pressure and capillary force are the main factors in terms of bulge shape.[20]

In terms of surface melting and polishing, Perry et al. proposed that the molten pool was a surface tension-driven capillary wave damped by viscosity.[23] Accordingly, the flow of the molten material was a balance between viscosity and surface tensions acting on the boundary between the molten metal and shielding gases. The temperature gradients across the melted pool resulted in surface tension differences that drove the flow of material outwardly, in the absence of surfactants.

By devising a two-dimensional numerical model that tied heat transfer with fluid flow, Zhang and others concluded that for a continuous wave (CW) laser surface processing, capillary forces dominate the molten pool at the initial stage of melting, while thermocapillary force becomes predominant when the molten pool fully develops.[24] Similar studies by Li et al. with a continuous wave (CW) fiber laser under the top-hat distributed heat source confirmed that the molten pool dynamics during the smooth process are primarily

governed by both capillary forces and thermocapillary forces, favoring one or the other based on surface topography and the viscous force's magnitude.[25]

In their work, Lee et al. examined the salient effects of thermocapillarity on the convective material flows of a laser cladding process.[26] They engineered a sophisticated, three-dimensional thermal-fluid model tailored to investigate the influence of sulfur in the melting pool during the Selective Laser Melting (SLM) processing of 316 powder.[27] The laser process utilizes higher power to compensate for the addition of material. Zhang et al. presented a model combining computational fluid dynamics and cellular automata.[28] They found the melt pool flow to be mainly driven by the competing Marangoni force and the recoil pressure on the liquid metal surface. Initially, high temperatures in the center of the laser spot and Marangoni flows bring the highest temperatures to the front side of the laser spot.

Additional knowledge must be developed for conduction micro-laser welding, in particular, when the initial conditions diverge from those of laser melting processes. Modeling more realistic welding environments for which the symmetrical conditions blur away, for instance, lacks research. When welding different materials, weldability depends on managing the disparity in the physical properties of dissimilar base materials, like heat conductivity or density. Some authors have developed simulation models for laser welding of different materials,[29–32] but more complexity in the form of geometrical asymmetry remains under researched. Dissimilar welds are marked by the differences in thicknesses, by preprocessing dissimilarities (e.g., welding cast versus forged parts), or by manufacturing variability, like misaligned parts.

Thus, welding in dissimilar conditions leads to asymmetric heat and material transportation. This technique has an impact on the weldment's geometry and, therefore, its quality. The laser beam location is conveniently offset from the joint and positioned at the lower weldability side, a well-known tactic to practitioners and academia [33–36] The heat input required to successfully execute the weld is brought to the
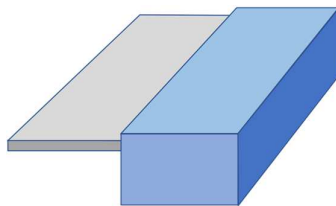
joint by the melting pool. See Figure 1 (c). The result shows an innovative way of laser micro welding

dissimilar parts while keeping absolute control of the melting pool. It further allows welding in areas where

the beam may not reach for geometric complexities, facilitating the work of mechanical designers and
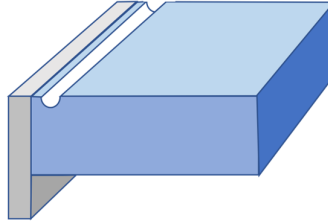
manufacturing engineers.
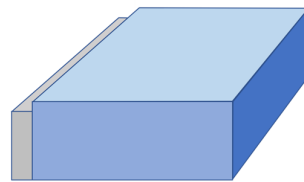
(a)
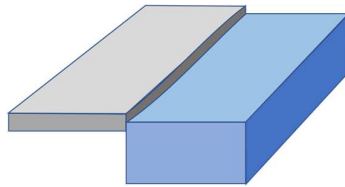
(b)

(c)

(d)

Figure 1. (a), (b) Dissimilar welding conditions by manufacturing variability (c) widely used method to offset beam to balance up weldability differences where the red dotted line represents the offset position, and (d) gouging to balance out heat input and weldability.

To understand more and eventually manage this intricacy, a multiphysics laser welding model that depicts the influence of these driving forces on weldment geometry has been developed using a commercially available multiscale multiphysics software tool. High energy density welding processes. like electron beam welding or laser beam welding have been recurringly simulated with multiscale multiphysics software. Huang et at. resorted to FLOW-3D for their numerical computations,[37] Borrmann and his colleagues fell back on free, open-source software, OpenFOAM,[38] and finally, Shcherbakov utilized for their computation a computer program developed in Microsoft Visual Studio.[39] Despite its costs in the high end, the selection of COMSOL comes as a result of the interest in incorporating several physics in the simulations, such as computational fluid dynamics and heat transfer modules, a user-friendly GUI and outstanding post-processing visualizations, a good interface with other software packages like MATLAB, and its intuitive interface allows non-experts to conduct rigorous, high-fidelity simulations.

An innovative geometry of the part is designed and embedded in this COMSOL environment to render the lateral displacement of the molten metal flows to understand and control the lateral zagging of this melting pool. Next to providing insights on dissimilar and asymmetric laser micro welding, the model permits an understanding of the effects of gravity and joint configuration design of the weld's geometry. The model's

validity and accuracy are demonstrated by showing a general agreement between the simulated and experimental results of the weld's cross-section. Its validity as a process optimization tool and its merit supporting for a Digital Twin are examined.

2. Mathematical Modelling of Laser Micro Welding

The mathematical model draws from the energy equation (eq. 1), the momentum equation (eq. 2) and the continuity equation (eq. 3), described, among many, by [24,40–42].

$$\rho C_p^* \left(\frac{\partial T}{\partial t} + v \cdot \nabla T \right) = \nabla \cdot (k \nabla T) + \rho L_f \frac{d f_L}{dt} \tag{1}$$

$$\rho \left(\frac{\partial v}{\partial t} + v \cdot \nabla v \right) = \nabla \cdot \left(-pl + \mu (\nabla v + \nabla^T v) \right) + F_v \tag{2}$$

$$\nabla \cdot u = 0 \tag{3}$$

where ρ is the liquid phase density, C_p is the specific heat, the asterisk, $*$ indicates values during the transition between solidus and liquidus, T is the temperature, t is the laser processing time, v is the velocity, k is the thermal conductivity, L_f is the latent heat of fusion, and f_L is the liquid fraction. Next, F_v is the volume force used to incorporate the effects of gravity.

$$F_v = F_g + F_b = \rho_0 g - \beta (T - T_{ref}) \rho_0 g \tag{4}$$

The liquid fraction f_L is assumed to vary linearly with temperature in the mushy zone (the phase distribution between liquidus and solidus temperatures) as follows:

$$f_L = \begin{cases} 1 & T > T_l \\ \frac{T - T_s}{T_l - T_s} & T_s \leq T \leq T_l \\ 0 & T < T_s \end{cases} \tag{5}$$

where T_s and T_l are the solidus and liquids temperatures, respectively. Furthermore, the modified heat capacity when solidus temperature is surpassed can be defined as:

$$C_p^* = L_m \frac{df_L}{dT} + C_p \qquad (6)$$

Since solid and liquid may coexist when the temperature exceeds the solidus temperature, mixed physical properties should be taken into consideration in this phase transition, which can be approximated as:

$$\alpha = f_l \cdot \alpha_l + (1 - f_l) \cdot \alpha_s \qquad (7)$$

where α_l is any physical property of the liquid phase and α_s is a physical property of the solid phase.

Then, liquid metal flow dynamic viscosity in both the mushy zone and solid part can be best described as:

$$\mu = [1 + (1 - f_L) \cdot A_{mush}] \cdot \mu_1 \qquad (8)$$

where A_{mush} is the mushy zone constant, a parameter used to simulate phase change effect on materials' physical properties. Values for the liquid dynamic viscosity as a function of temperature are collected in Table 1.

Table 1. Dynamic Viscosity Values for AISI 316L[43]

Temperature (K)	Viscosity (cP)	Temperature (K)	Viscosity (cP)
1700	6,42	2400	2,50
1800	5,36	2500	2,28
1900	4,57	2600	2,10
2000	3,95	2700	1,94
2100	3,47	2800	1,80
2200	3,08	2900	1,69
2300	2,76	3000	1,58

In autogenous, conduction laser micro-welding, surface forces govern the hydrostatic front. Capillary forces act in the normal direction, while the Marangoni flows do so tangentially. A body force, gravity, may be introduced in dissimilar joint geometry welding conditions as heat transfer characteristics vary. Capillary forces normally originate at the interface between two immiscible fluids, like molten metals and shielding gas used for micro-welding. The surface tension is highest near the solid-liquid interface (at lower temperature regions), driving the transfer of heat and material from the center to the periphery of the weld.[44] Next to welding parameters, both the joint configuration and manufacturing variability affect as well the melting pool size and its shape.

$$\sigma = \gamma \boldsymbol{n}(\nabla \cdot \boldsymbol{n}) - \nabla\gamma = \boldsymbol{\sigma_n} - \boldsymbol{\sigma_t} \tag{9}$$

where σ_n is the normal stress, σ_t is the tangential stress on the surface and γ is the surface tension.

3. Computational Model for Asymmetric Laser Micro Welding

A 2D transient, axisymmetric model is created with COMSOL 6.2 Multiphysics software package to simulate the light-matter interaction of a continuous wave laser source with an asymmetric edge weld made of standard AISI 316L stainless steel. A calculation domain with geometric dimensions of 1000 µm x 1200 µm is proposed. A 20 µm step, up and down, is included to simulate a mispositioned tube and observe its effect on the pool hydrodynamics. The tube and socket become attached to each other immediately after welding begins. An alternative geometry from which a piece of the block is removed to create lateral free surface and allow flow laterally is proposed. This modeling strategy allows the material to up well, perpendicularly to the free surface, displaying the influence of gravity on both thermocapillarity and capillarity. It further acts as a heat sink to capture additional heat and incorporates the effect on heat absorption by existing parts not included in the model. The proposed geometry illustrates how these three driving forces interact, forming a geometry upon melting.

The free surface motion is tracked by using the *ALE* method, which relies on the *Free Surface* and the *Moving Mesh* options. The velocity field computations are calculated from the Navier-Stokes equations. All geometry boundaries are allowed to exhibit both natural convection and radiation behavior. The laser is fed through a small portion of boundary 4, to account for the effects of a positioning offset. This area is selected to be relatively small to model a high-quality laser with a beam propagation ratio of M^2 <1.1 and to facilitate the model's convergence. The laser density in W/m^2, depicted as a moving source, is the product of the laser energy absorptivity in the material times the energy density and the exponential term, representing the Gaussian laser beam distribution. The laser flux distribution is a function of space (r, z, t) for a 2D axisymmetric simulation. Since the laser spot size is not near its wavelength (1073 nm), the Gaussian beam formulation is appropriate. The continuous wave laser source, modeled as a Gaussian beam with TEM_{00},[45] emits enough energy to melt a discrete amount of material that matches the material's latent heat of fusion.

$$I(r,z) = A \cdot \frac{P}{\pi z^2} \cdot exp\left(-\frac{(r-r_t)^2}{2\phi^2}\right) \tag{10}$$

where P is the power in W, P_w is the pulse length (1 for continuous wave), r and r_t are the beam position along the part as time progresses, D is the beam diameter, and ϕ is the Gaussian beam standard deviation, or the beam radius divided by four.[46]

The *Free Surface* feature is activated in combination with this temperature-dependent surface tension, instead of the Marangoni effect in the Multiphysics section, to simulate thermocapillarity. It also addresses capillarity by including a contact angle in the hydrophobic range to represent the iron behavior in the presence of inert gases. The moving mesh prescribes the displacements at boundaries 5, 6, 7, and 8 shown in Figure 2, which displays the mesh strategy for three different cases in terms of alignment.

The number of degrees of freedom solved for is 67037 (plus 17661 internal DOFs) and used 3 hours and 48 minutes of computing time.

Table 2. Boundary Conditions

Physics	Constraints	Boundary #	Boundary Condition
Heat Transfer	Laser Heat	4	
	Convection	1,2,3,4,5,6,7,8	
	Radiation	1,2,3,4,5,6,7,8	
Laminar Flow	Normal Stress	1, 2, 3, 4	Free Surface
	Tangential	1,2	Free Surface
	Wall	6	Non-slip Wall
	Wall 2	1, 2, 3, 4	Navier Slip

|			
	Free Surface	1,2,3, 4, 8	Free slip
Moving Mesh	Fixed	5, 7, 8	
	Free	1, 2, 3, 4	

The meshing consists of minuscule, rectangular elements near the top calibrated for fluid dynamics for accuracy, displayed in Table 3. The rest of the mesh elements are of fine size since they are irrelevant for calculations. Figure 2 depicts the boundary conditions and the mesh strategy.
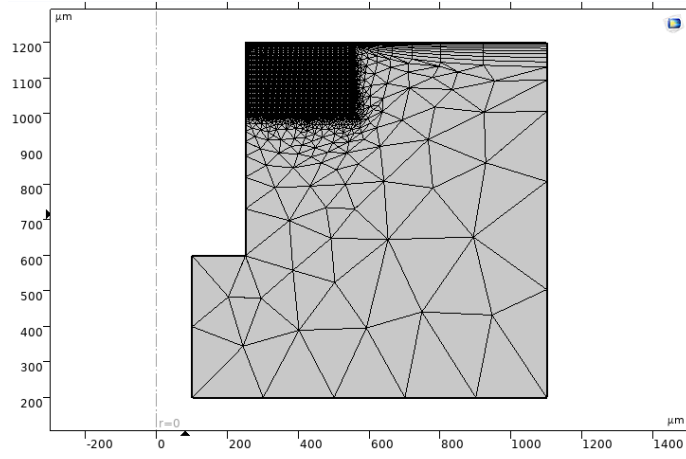
Table 3. Element Size Parameters

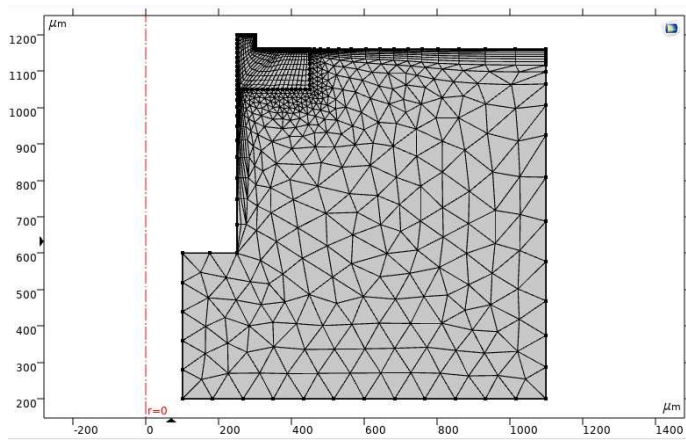| Parameter (unit)	Domain of Interest	Rest
Maximum Element Size	3.35 µm	220
Minimum Element Size	0,01 µm	7 µm
Maximum Element	1,025	1,4
Curvature Factor	0,2	1
Resolution of Narrow	1	0,9
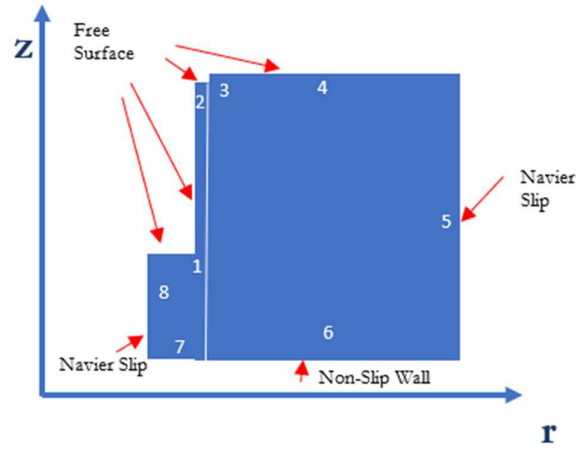
(a)
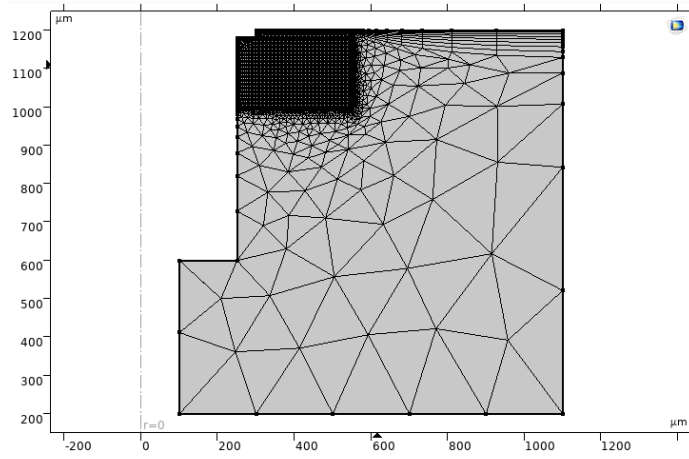
(b)

(c)

(d)

Figure 2. (a) COMSOL geometry (b), (c) and (d) meshing strategies to represent possible manufacturing variability and different meshing strategies for it

Finally, Table 4 highlights the thermophysical properties of AISI 316L.

Table 4. Thermo-physical Properties of AISI 316L

Parameter	Nomenclature	Value	Ref.
Density [kg/m³]	ρ	7500	[47]
Specific Heat of Solid Material [kg/m·s]	C_p	462.656+0.1338T	[47]
Specific Heat of Liquid Material [J/kg·K]	C_p	776	[47]
Thermal Conductivity of Liquid Material	k	12.41+3.279E-	[47]
Thermal Conductivity of Solid Material	k	9.248+1.571E-	[47]
Ambient Temperature [K]	T_a	293,15	
Melting Temperature [K]	T_m	1660.65	
Boiling Temperature [K]	T_b	3086	[48]
Solidus [K]	T_s	1648,15	[40]
Liquidus [K]	T_l	1673,15	[40]
Surface Tension [N/m]	σ	3.282-8.9E-04·T	[48]
Temperature Derivative of Surface Tension	$\partial\sigma/\partial T$	0.4E-03	[48]
Latent Heat of Boiling [J/kg]	L_b	6.1E6	[48]
Latent Heat of Melting [J/kg]	L_m	2.8E5	[48]
Mushy Zone Constant	A_{mush}	10E7	[40]
Absorptivity	a_0	0,50	[49]

4. Experimental Setup

Three samples of 316L tube and a MIM 316L socket are laser welded in a vertically transmitted Rofin IPG
fiber laser with a wavelength of 1073 nm and a maximum output power of 200 W, delivering continuous

wave (CW). The tube thickness is 50 μm, and the internal and external diameters for both tubes and sockets are 250 and 300 μm. The thermophysical properties of MIM 316L are assumed to be the same as those of the 316L tube. The laser welding parameters, maintained fixed during the experiment to isolate them from the variable of the study, are 26.75 W, CW, 9 mm/s, and a 310 mm offset. Shielding argon (99.99%) was ejected through a co-axial 20 mm nozzle. A Bronkhorst High Tech Flexi-Flow gas flowmeter was used to accurately manage the 15L/min argon protection. Tubes are mispositioned artificially to demonstrate the weldment's sensitivity to initial conditions. A post-solidification macrograph displaying actual welding morphology was created against simulated welding profiles. For this purpose, a Struers sample cutting device was used to prepare the specimens and, after etching and polishing, a VHX-7000 Keyence microscope with up to x1000 magnifications was utilized to evaluate them and document the results.
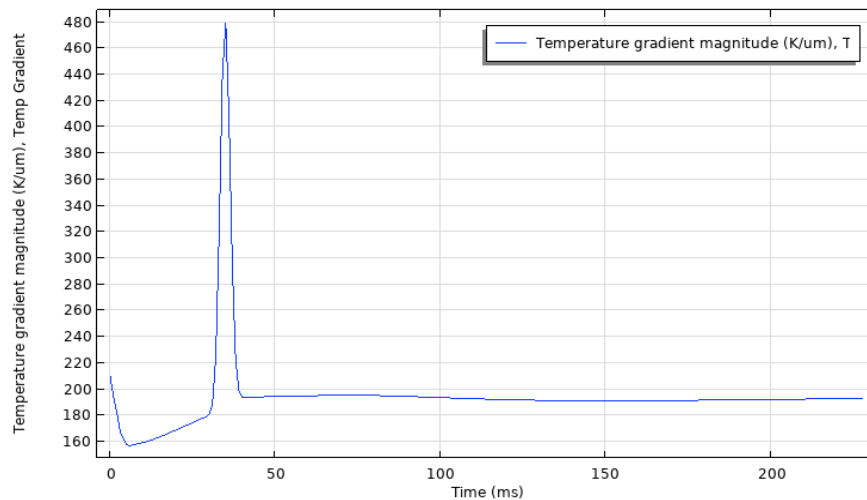
5. Results, Analysis and Discussion

Figure 3 illustrates the experimental and simulated results when the two parts are deliberately mispositioned to depict manufacturing variability for the experiment. An arbitrarily chosen cross-section, slightly away from the starting point, represents the welding analysis area. As the laser approaches this point and interacts with the metal, energy absorption increases its temperature until it progressively melts. The molten metal, per the capillary action exerted in the normal direction, accumulates in a sessile droplet, often referred to as a bulge, whose dimensions depend on the contact angle and interfacial surface tension. Figure 3 (a) displays the temperature gradient along the melting and solidification cycle at a randomly chosen point, while Figure 3 (b) represents the moment the beam passes through the randomly selected cross-section. Both indicate a peak that coincides in time.
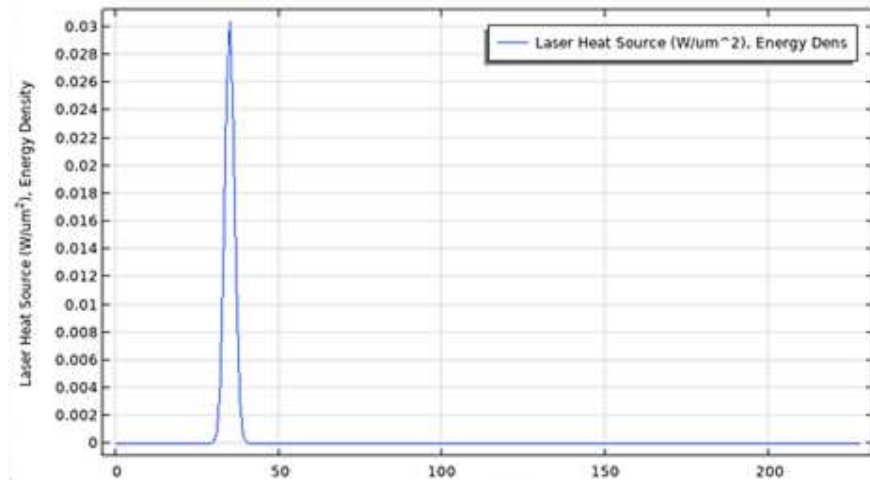
This bulge remains stationary until the laser beam travels over the analysis area. Then, the maximum power density is delivered. The power, concentrated over a minuscule area per beam spot size, generates the

maximum temperature gradient, triggering local surface tension differences and thermocapillarity to balance it out. At this particular instant, t=35 ms, thermocapillarity circulates the molten metal from the center to the periphery of the weld, aided by gravity as the pool descends through the part misalignment. Consequently, the existing temperature differences quickly dissipate when thermocapillarity stirs the molten pool, substantially slowing it down. A marginal value prevails along the welding cycle. Figures 3 (c) and (d) depict the phase and the velocity, respectively, as the pool evolves when thermocapillarity peaks, revealing the high energy density nature of the process.
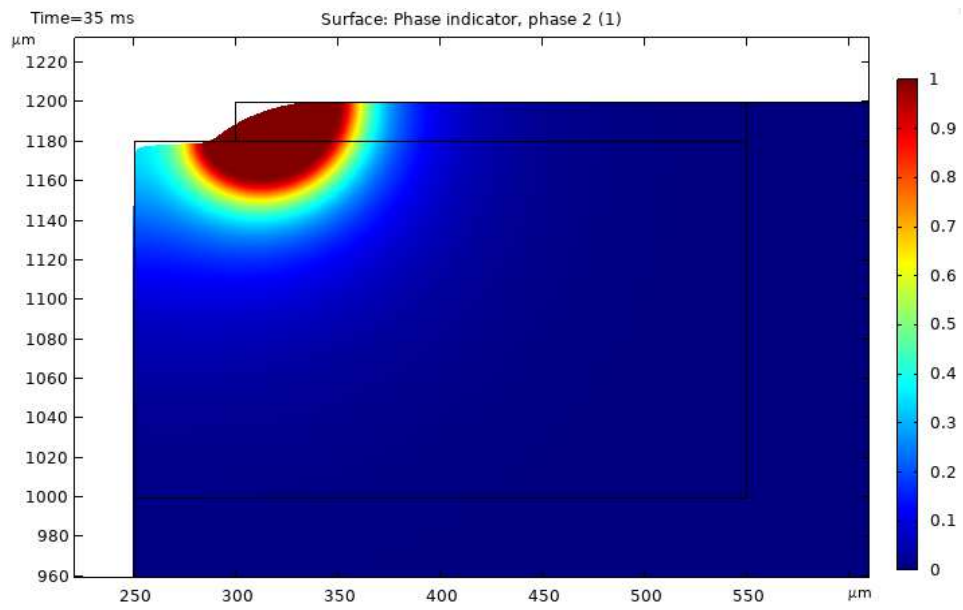
Although they coexist to a certain extent, if a temperature gradient is large enough, thermocapillarity annuls capillarity. Figures 3 (e) and (f) show the status long after the beam has passed through the area of interest and the melted pool is idle. Figures 3 (e), (f), and (g) display the final welding geometry at t = 218 ms when the metal is still liquid, as the phase graphs show, but exhibits no motion and, therefore, no further geometry alteration can ensue. This shape is then final. At this precise moment, the laser source has completed the weld. Finally, Figure 3 (h) shows how the tube and socket become attached immediately after welding starts, enlightening the assumption that no gap between the welding parts exists. This sequence, repeated successively across the joint, constitutes the full weld.
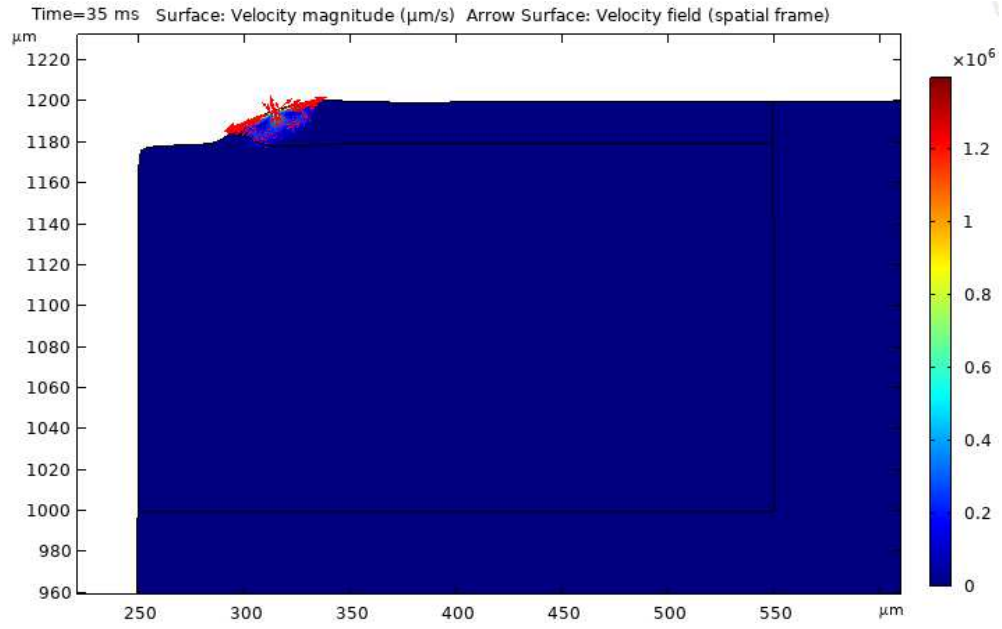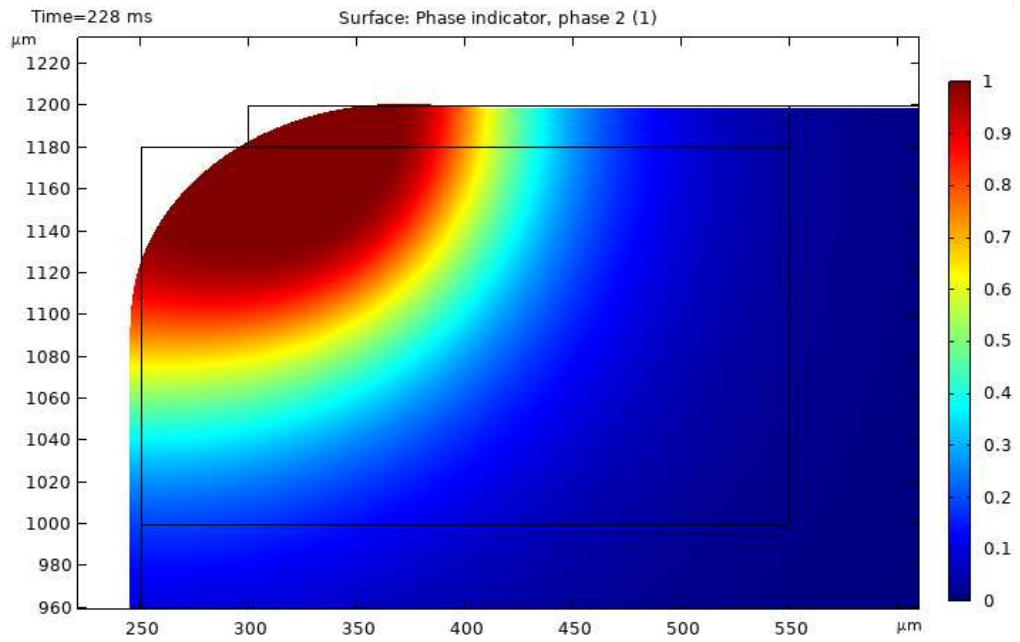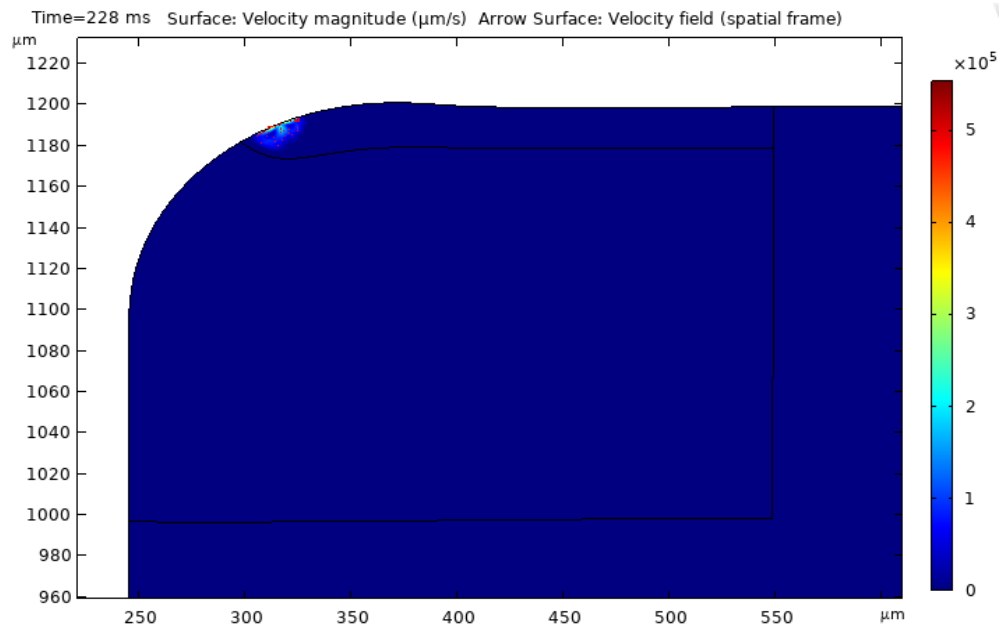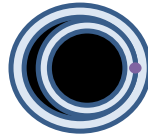
(a)

(b)

(c)

Time=35 ms   Surface: Velocity magnitude (μm/s) Arrow Surface: Velocity field (spatial frame)

(d)

Time=228 ms   Surface: Phase indicator, phase 2 (1)

(e)

Time=228 ms   Surface: Velocity magnitude (µm/s) Arrow Surface: Velocity field (spatial frame)
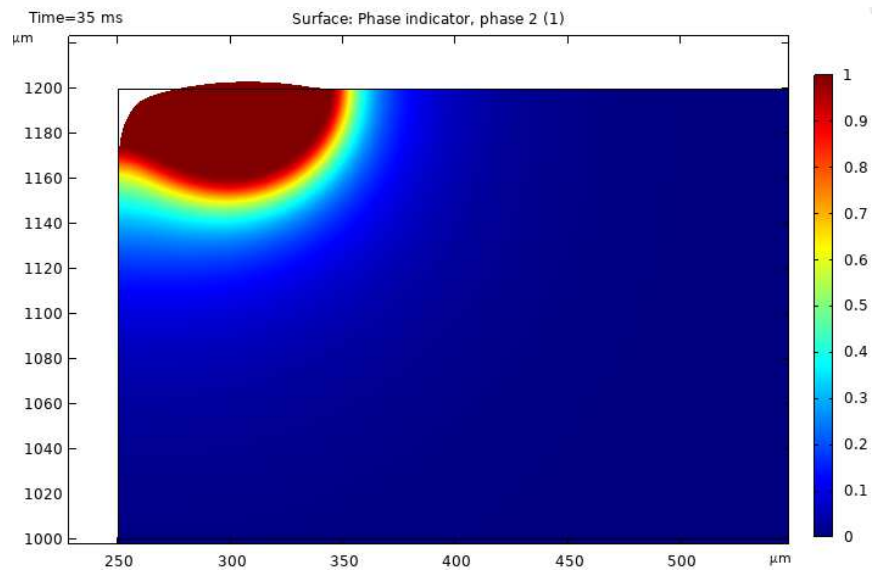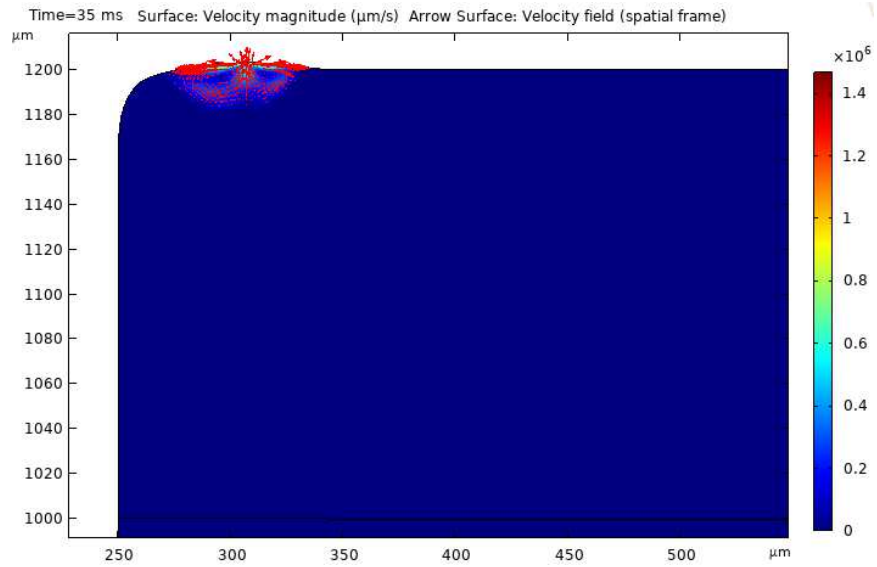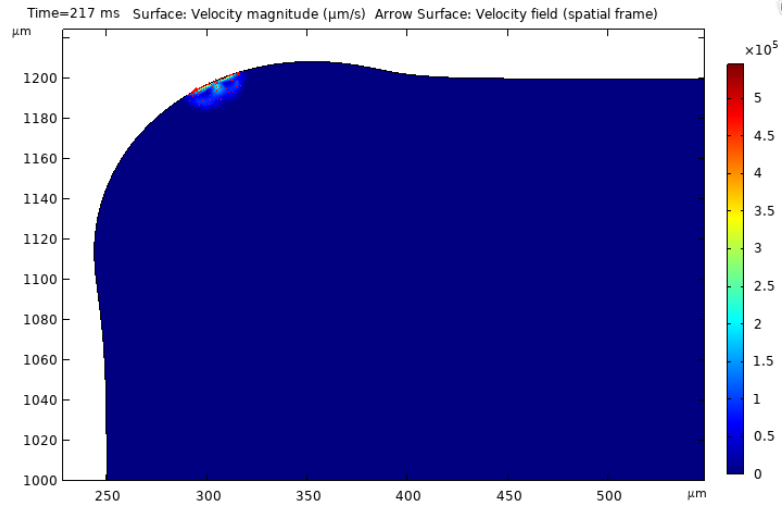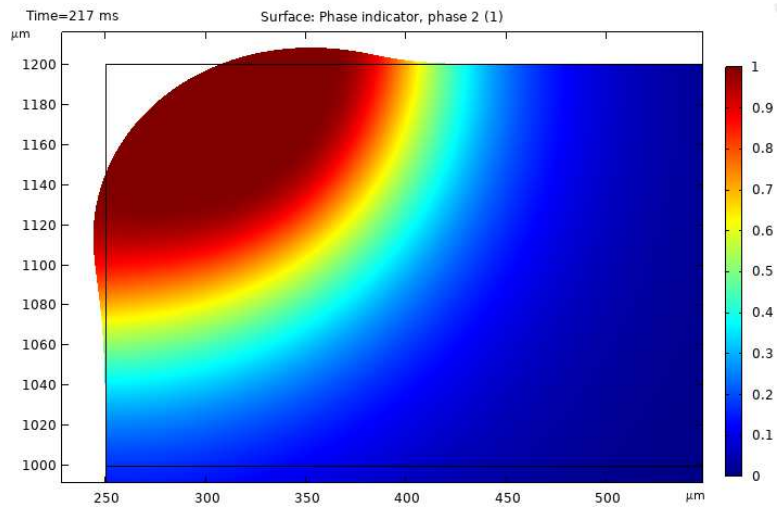
(f)

(g)

(h)

Figure 3. (a) Temperature gradient through laser welding cycle (b) laser energy density, (c) Phase distribution at maximum thermocapillarity (d) Maximum speed at maximum thermocapillarity (e) phases after complete laser cycle at t=228 ms (f) idle pool at the end of laser cycle at t=228 ms, and (g) actual weld profile replicating conditions, published with the permission of Bronkhorst High Tech at the same scale of simulated results, and (h) position of tubes as weld begins.

A compelling scenario unfolds when these two parts to be welded align perfectly, as depicted in Figure 4. The laser beam offset position is adjusted to accommodate the surplus material while keeping the welding parameters constant. The pool evolves in distinct phases. Initially, depicted in Figure 4 (a) and (b), as heat is delivered and the metal melts, the pool size grows, and, as a consequence of capillarity, a droplet dominated by normal forces develops. As the beam passes by the arbitrarily selected point, gravity, in combination with thermocapillarity, becomes predominant and flattens the droplet, as discussed in Figure 3. The pool shifts toward the outer side, where the temperature difference peaks, facilitating the convective heat transfer process. Finally, gravity overcomes the strength of the droplet surface energy, and materials and energy flow toward the edge. Metal accumulates in a bulge as the laser beam has passed the area of interest. The final gravity-capillarity interaction before solidification determines the final geometry of the weld in Figure 4. This case, next to demonstrating the external rendering of the material, further supports the thesis that when temperature gradients subside, capillarity comes to the forefront and forms a bulge.

Time=35 ms   Surface: Velocity magnitude (µm/s) Arrow Surface: Velocity field (spatial frame)

(a)

Time=35 ms   Surface: Phase indicator, phase 2 (1)

(b)

Time=217 ms   Surface: Velocity magnitude (μm/s)   Arrow Surface: Velocity field (spatial frame)

(c)

Time=217 ms   Surface: Phase indicator, phase 2 (1)

(d)

(e)

Figure 4. (a) Maximum thermocapillarity at t=35 ms, (b) Phases present at maximum thermocapillarity at t=35ms, (c) Phase distribution at t=217 ms, (c) Idle pool at the end of laser cycle at t=217 ms (e) Final results, published with the permission of Bronkhorst High Tech at the same scale of simulated results.

A third case is still possible, when the two parts to be welded are misaligned and the tube is higher. In the debate about the influence of capillarity and thermocapillarity on the geography of the weld, this study shows that the initial conditions have a major impact on the melting pool evolution. Concretely the topology of the area before welding, the tortuosity of the path that the melting pool encounters on its way influence as well the weldment's geometry. In this specific case gravity cannot support hydrodynamics as there is a geometrical impediment that previously was not there: the tube. Yet some of the common themes like mushy zone reduction when the thermocapillarity is acting and maximum. Also, the peak thermocapillarity occurs at t=48 ms, when the maximum temperature and surface tension gradient take place.
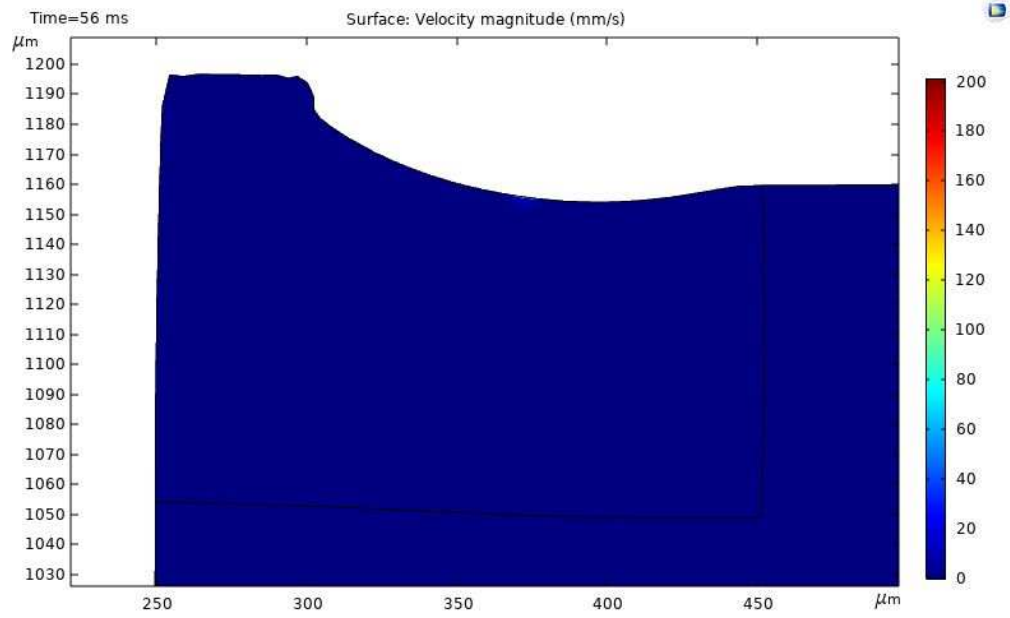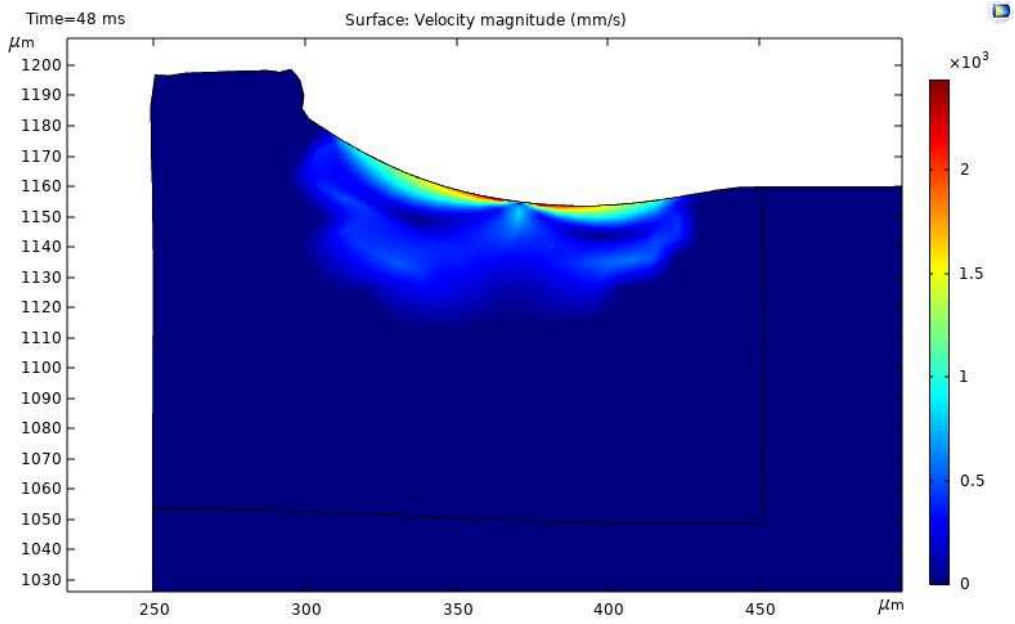
(a)

(b)
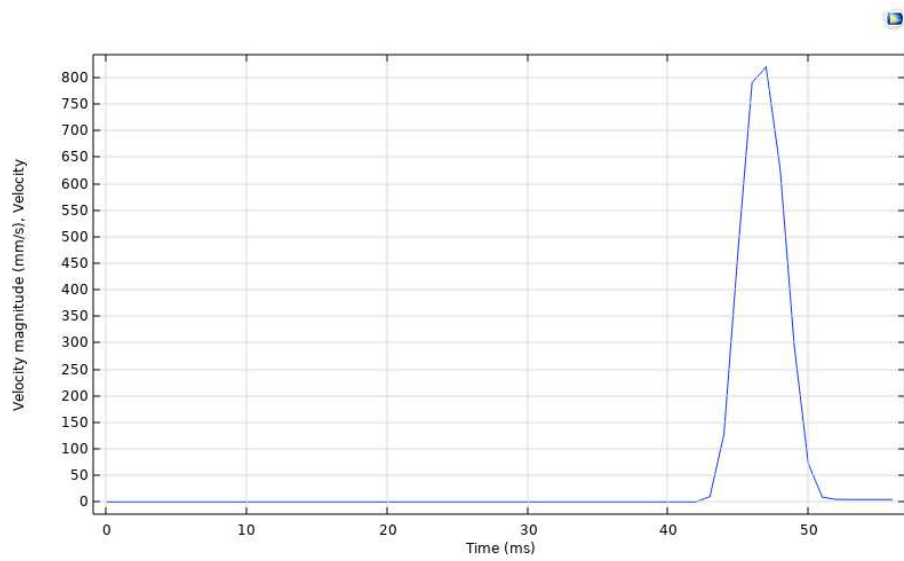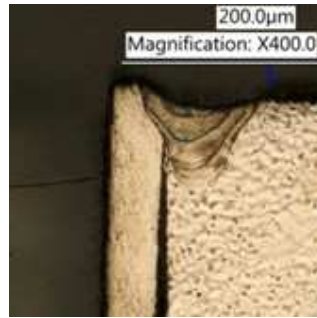
(c)

(d)

Time=48 ms — Surface: Velocity magnitude (mm/s)

(e)

200.0μm
Magnification: X400.0
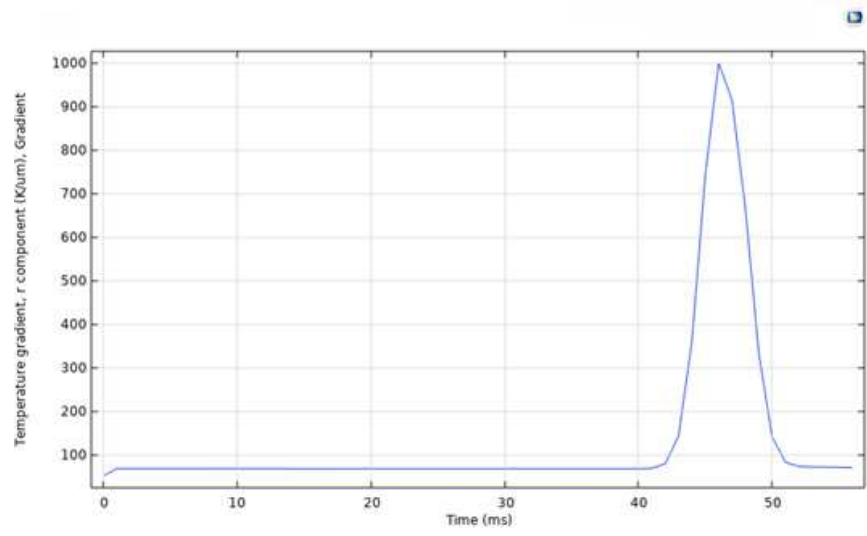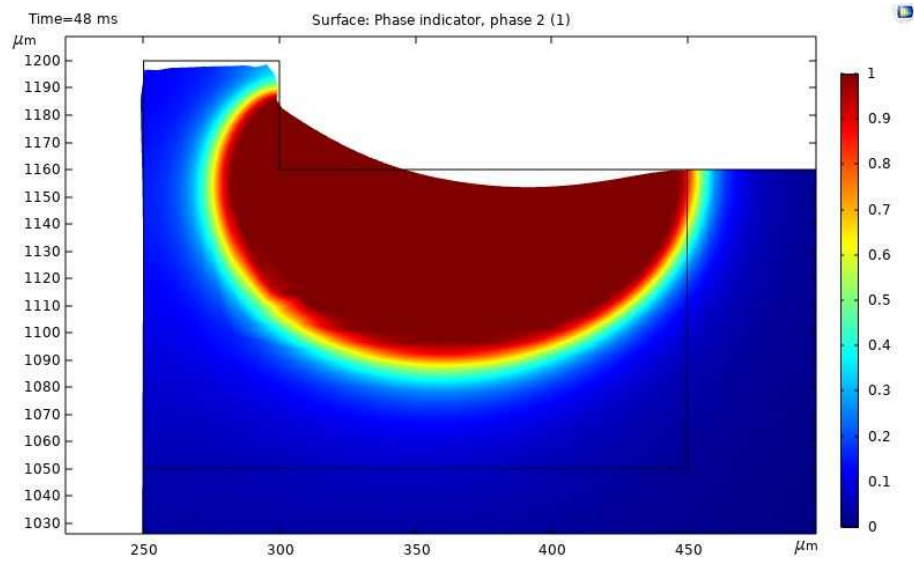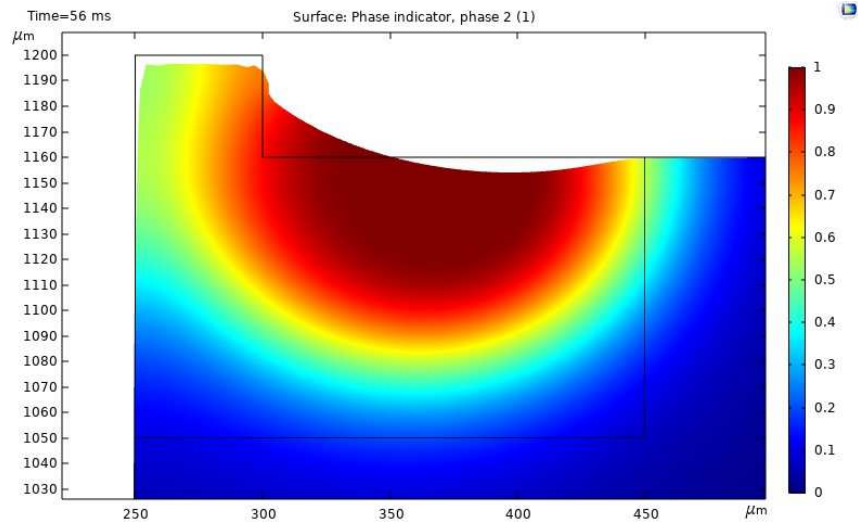
(g)

Figure 5. (a) Another possibility of weld configuration by manufacturing variability, this photo shows the temperature gradient, indicating when the highest thermocapillarity occurs (b) Last liquid present at maximum thermocapillarity at t=48ms, (c) Phase distribution at t=56 ms, when the poodle cannot change its geometry anymore (d) Idle pool (no speed) at the end of laser cycle at t=56 ms (e) moment in which the speed is maximum and it occurs at t = 48 ms, (h) surface tangential velocity, displaying a maxima wen t=48ms (g) Final empirical results displaying high fidelity with Figures 5 (b), (c), (d), and (e), published with the permission of Bronkhorst High Tech, at the same scale of simulated results.

Numerous studies in the literature support the strength of these laser micro welding simulation findings. As an instance, Yang et al. have suggested that during the heating stages of laser melting, the flow of molten metal is primarily influenced by capillary and thermocapillary forces, whereas during the cooling phase, capillarity becomes the dominant factor.[20] These results show complete consistency with these views. Aligned with this present work, Zhang et al. have argued that capillary forces dominate during the heating phase, while thermocapillarity becomes prominent as the molten pool fully develops.[24] In their study on pulsed wave laser melting, Vadali, and his colleagues also made a corroborating observation: longer pulses have a more substantial influence on Marangoni convective flows. This phenomenon is attributed to the extended pulse duration, which leads to a greater volume of molten material, allowing sufficient time for

surface tension forces to overcome reduced viscous forces, resulting in the development of convective flows.[50] This study, with continuous wave laser welding, confirms the veracity of these results.

Li et al.[25] have also acknowledged the significant contributions made by both thermocapillarity and capillarity. Capillarity smooths out prominent surface irregularities, such as peaks, while thermocapillarity generates tangential flows that improve surface quality. As this effect continues over an extended period, the decline in roughness becomes increasingly evident. This prediction is aligned with experimental results and holds for most metal surfaces. A similar phenomenon has been reported in laser cladding, where the addition of material introduces new insights into flow hydrodynamics. Marangoni convection induces heat flow, as shown by the flat temperature gradient profiles. Behind the laser beam, in the zone with the most penetration, surface tension gradients, both positive and negative, contribute to deeper penetration. Convection plays a pivotal role in this hydrodynamics setting.[26] Notably, in their exploration of chemo-capillarity, Shen et al. identified a pivotal temperature threshold within the melting pool, suggesting that lower energy input into the weld resulted in a prevailing radial inward flow. Thermocapillarity governs during the heating stages, whereas capillarity becomes dominant during the cooling period.[40] The latter statement agrees with the results of this work. But this idea admits a refinement that removes the heating and cooling stages. Thermocapillarity dominates over capillarity whenever there is a local surface tension gradient.

Remarkably, during the concentration of molten metal as a consequence of capillarity, the mushy zone, where liquid and solid coexist at varying proportions, is initially extensive and deep. However, as thermocapillarity comes into play for differences in surface tension, this mushy zone diminishes to a minimal extent as the bulge extends. Capillarity, on the other hand, promotes the depth of the mushy zone. See the difference between Figure 5 (c) and Figure 5 (d). This observation could provide a significant insight into the mechanism behind the formation of cracks in laser micro welding of austenitic stainless steels and should be studied further. A forthcoming article by the authors deals with this finding.

Figures 3, 4 and 5 show the model is capable of reproducing empirical tests with precision. Additional findings indicate that the model can calibrated when selecting appropriate values for A_{mush} is high enough to assure flow, and the viscosity value for the solid phase of the part is sufficient to prevent its fictive, non-existent fluid motion at the solid phase. The appropriate selection of these two variables assures the model's convergence and its fidelity.

About mapping welding flaws in laser micro-welding, apart from cracks, which often result from high cooling rates and sulfur concentrations, defects can also arise from manufacturing variations associated with initial conditions. These defects may manifest when the melting pool excessively wets the parts (as shown in Figure 4) or fails to wet them sufficiently (as illustrated in Figure 5), primarily due to the hydrodynamic characteristics involved. The correct sequence of capillarity and thermocapillarity and, in particular, their magnitude and direction determine laser micro-welding quality for a given manufacturing tolerance. Factors influencing welding defects are those that either inhibit or enhance Marangoni convection. These elements encompass beam offset distance, which can drive convective heat and material transfer, power affecting droplet size, spot size influencing thermocapillarity strength, and speed impacting both the width of the melting pool and the level of freedom at its surface. Hence, restricting the diameters of laser focal spot sizes leads to increased temperature gradients and more robust Marangoni flow convections. Defocusing the beam would result in the opposite effect. Supplying higher power or programming slower scanning speeds would induce larger pools and, therefore, a substantial capillarity effect.

The minor variations in weldment geometry observed between experimental and simulated outcomes can be attributed to the impact of sulfur or other surfactants. These surface-active substances may generate inward radial surface forces, which can sometimes prevail over the outward radial forces caused by thermocapillarity. This type of flow convection, commonly referred to as chemo-capillarity, is a well-known phenomenon in the welding of austenitic stainless steels. For the present study, the numerical values

of surface tension have been expressed only in terms of temperature. While formulas of surface tension in terms of both temperature and sulfur concentration exist in the literature, [51] for this work, since it is oriented towards high-value industries, the sulfur concentration factor is excluded from it. These industries impose stringent sulfur content standards on suppliers dealing with austenitic stainless steels, precisely, to enhance the welding process. Although achieving 100% sulfur-free stainless steel isn't feasible, this simplifying assumption has been validated by the experimental results. One final noteworthy factor contributing to uncertainty in this modeling process is the material's capacity for light absorption. Heterogeneities in the surface quality, accentuated by joining two materials with dissimilar surface quality, compound the value of laser power absorptivity. Lower thermal conductivity likewise lessens the temperature gradient at the surface, leading to a decrease in the outward heat convective flows and, consequently, causing a reduction in the width of the weld.[52] Ultimately, the surface heat source featuring an ideal Gaussian energy distribution stands out as a key factor contributing to the discrepancies observed between experimental and simulated trials. Another issue is the calibration of the model by playing with A_{mush} values and the artificial value of solid viscosity. The correct selection of these values not only assures the model's convergence but also the fine-tuning of the weldment's geometry. This can raise some doubts about the physical significance of these changes.

Despite these limitations, this modeling and analysis approach remain capable of furnishing mechanical designers with a robust sensitivity analysis tool, enabling them to uncover ideal values for critical process variables and effectively prevent defects at the design stage. The high-fidelity model can be of benefit as a process optimization tool. By conducting a simplified design of experiments, it is possible to identify the optimal parameter and tolerance design. Determining a maximum and minimum value for an offset of the laser beam indicates, for instance, the size of the gap and its tolerance to manage the number of defective welds. In terms of system design, and given a specific weldment design, the model can provide important clues to the mechanical design engineer concerning power, spot size, or speeds needed to create the desired

welding geometry. The system, which is the equipment and a fine-tuned welding process itself, can be intentionally built with this objective in mind. The advantages of having this information at the product design phase favor greater success chances at the various industrialization phases.

To conclude, real-time laser signal processing is a well-developed technique to pinpoint laser welding process anomalies that typically identify defects. Misalignments, for instance, can be identified during real-time monitoring using optical sensors by capturing laser back reflection light.[53] The weld's depth can be measured by measuring acoustic signals.[54] A Digital Twin, DT, utilizes these in-situ collected data and enters it into a multiscale model based on first principles to predict welding quality similar to the one proposed in this work. Mapping the welding defects and sequencing hydrodynamics (i.e., thermocapillarity and capillarity) that lead to defects can result in a deeper understanding of the root cause of these defects. A welding defect antecedent is an anomaly that precedes the occurrence of a welding defect. Identifying these antecedents by interpreting laser processing signals, a DT could act on them by altering the driving forces. High computation costs, however, deem its applicability for a real-time operating Digital Twin unfeasible. In terms of Digital Twins, the main merit of the model presented in this work is the hydrodynamics understanding. This knowledge can substantially aid in developing a hybrid model that involves a form of Big Data analysis technique, such as Machine Learning. Albeit it is still further investigated by the authors and to be published separately.

6. Conclusions

This article addresses conduction micro-laser welding with lower power and speed conditions. A model is created in COMSOL to find the process' peculiarities and compare it to experimental results. The work describes an innovative way to laser micro-weld plates or tubes with asymmetric, dissimilar weldabilities. This technique allows welding in areas where the laser beam may not reach by assuring the melting pool

brings the necessary heat input. Only three variables are required to manage a specific welding system: a new variable, offset, power, and speed. The main findings of the present work suggest that, at the onset, capillarity creates a reservoir of molten material in the form of a bulge, which acts as a sink of convective heat that ultimately thermocapillarity distributes both along the joint. Thermocapillarity governs hydrodynamics over capillarity whenever there is a local surface tension gradient. The article further contends that the joint configuration, the topology, and gravity influence the geometry of the weld. Additional findings come from the Smart Manufacturing perspective. If capillarity and thermocapillarity are the determining factors for weldment geometry, then skillful management of these forces presents a promising avenue for maintaining online weld quality. Different defects have different melting pool evolution. An appealing future research is the role of both capillarity and thermocapillarity on the mushy zone, a weldment zone that influences its crack tendency. Therefore, to understand the phenomena leading to a determined weldment geometry and become part of the predictive features of a Digital Twin, the hydrodynamics leading to welding defects must be mapped to become part of the predictive features of a Digital Twin. Nevertheless, the significant computational expenses pose a hindrance to integrating this model into a Digital Twin system. Forthcoming research must incorporate AI and data analysis techniques in hybrid models that combine them with multiphysics model findings. From the process design perspective, capillarity and thermocapillarity actions can be orchestrated offline, at the parameter design phase, to obtain a desirable hydrodynamics outcome leading to the correct quality levels. Its suitability to support system, parameter, and tolerance design is assessed and deemed appropriate. Ultimately, the model can accurately replicate the experimental tests, including the internal zagging of the material.

Conflict of Interest

The authors declare that there is no conflict of interest.

References

1. Cheng K, Huo D. Micro Cutting: Fundamentals and Applications. Chichester, West Sussex, United Kingdom: Wiley, 2013. Epub ahead of print 2013. DOI: 10.1002/9781118536605.

2. Semak VV, Hopkins JA, McCay MH, et al. Melt Pool Dynamics During Laser Welding. Journal of Physics D: Applied Physics 1995; 28: 2443. DOI: 10.1088/0022-3727/28/12/008

3. Fotovvati B, Wayne SF, Lewis G, et al. A Review on Melt-Pool Characteristics in Laser Welding of Metals. Advances in Materials Science and Engineering 2018; 2018: 4920718. DOI: 10.1155/2018/4920718

4. Rahim Abadi SMAN, Mi Y, Sikström F, et al. Influence of Laser Beam Shaping on Melt Pool Thermocapillary Flow. In: Proceedings of the 6th World Congress on Mechanical, Chemical, and Material Engineering, pp. 1–9. DOI: 10.11159/htff20.125

5. Wang B, Hu SJ, Sun L, et al. Intelligent Welding System Technologies: State-of-the-Art Review and Perspectives. Journal of Manufacturing Systems 2020; 56: 373–391. DOI: 10.1016/j.jmsy.2020.06.020

6. Ebrahimi A, Kleijn CR, Richardson IM. Numerical Study of Molten Metal Melt Pool Behaviour During Conduction-Mode Laser Spot Melting. Journal of Physics D: Applied Physics 2020; 54: 105304. DOI: 10.1088/1361-6463/abca62

7. Velázquez de la Hoz JL, Cheng K. Development of an Intelligent Quality Management System for Micro Laser Welding: An Innovative Framework and Its Implementation Perspectives. Machines; 9. 2021. DOI: 10.3390/machines9110252.

8. Ayoola WA. Parameters Controlling Weld Bead Profile in Conduction Laser Welding. Journal of Materials Processing Technology 2017; 9. DOI: 10.1016/j.jmatprotec.2017.06.026

9. Rajulu CG, Krishna AG, Babu Rao T. An Integrated Evolutionary Approach for Simultaneous Optimization of Laser Weld Bead Characteristics. Proceedings of the Institution of Mechanical Engineers, Part B: Journal of Engineering Manufacture 2018; 232: 1407–1422. DOI: 10.1177/0954405416667431

10. Shah D, Sewatkar CM, Godbole K. Numerical Analysis of Heat Transfer and Fluid Flow in Micro-Welding Using CFD. In: ASME International Mechanical Engineering Congress and Exposition. American Society of Mechanical Engineers, 2018, p. V007T09A066. DOI: 10.1115/IMECE2018-86363

11. Noori Rahim Abadi SMA, Mi Y, Sikström F, et al. Effect of Shaped Laser Beam Profiles on Melt Flow Dynamics in Conduction Mode Welding. International Journal of Thermal Sciences 2021; 166: 106957. DOI: 10.1016/j.ijthermalsci.2021.106957

12. Xiao X, Lu C, Fu Y, et al. Progress on Experimental Study of Melt Pool Flow Dynamics in Laser Material Processing. In: Liquid Metals. IntechOpen, DOI: 10.5772/intechopen.97205 (2021).

13. Schöler C, Nießen M, Hummel M, et al. Modeling and Simulation of Laser Micro Welding. In: Lasers in Manufacturing Conference. 2019.

14. Patel S, Aggrawal A, Kumar A, et al. Micro Laser Lap Welding of Thin SS304 Sheet. In: Lasers in Manufacturing Conference. 2019.

15. Wu J, Zhang H, Feng Y, et al. 3D Multiphysical Modelling of Fluid Dynamics and Mass Transfer in Laser Welding of Dissimilar Materials. Metals; 8. Epub ahead of print 2018. DOI: 10.3390/met8060443.

16. Shah A, Kumar A, Ramkumar J. Analysis of Transient Thermo-Fluidic Behavior of Melt Pool During Spot Laser Welding of 304 Stainless-Steel. Journal of Materials Processing Technology 2018; 256: 109–120. DOI: 10.1016/j.jmatprotec.2018.02.005

17. He X, Elmer JW, DebRoy T. Heat Transfer and Fluid Flow in Laser Microwelding. Journal of Applied Physics 2005; 97: 084909-084909–9. DOI: 10.1063/1.1873032

18. Patel S, Aggrawal A, Kumar A, et al. High-Speed Conduction-Mode Micro-Laser Welding of Thin SS-304 Sheets: Modeling and Experimental Validation. In: Shunmugam MS, Kanthababu M (eds) Advances in Micro and Nano Manufacturing and Surface Engineering. Singapore: Springer Singapore, 2019, pp. 153–165. DOI: 10.1007/978-981-32-9425-7_13

19. Sharma S, Ramakrishna SA, Ramkumar J. Numerical Simulation of Melt Hydrodynamics in Laser Micro Processing of Metals. Procedia CIRP 2020; 95: 944–949. DOI: 10.1016/j.procir.2020.01.186

20. Yang X, Fu Y, Ji J, et al. Study on the Influence of Capillary Force and Thermal Capillary Force on Surface Bulge Morphology by Laser Micro-Melting. Transactions of the Indian Institute of Metals 2022; 75: 727–735. DOI: 10.1007/s12666-021-02430-3

21. Buttazzoni M, Zenz C, Otto A, et al. A Numerical Investigation of the Laser Beam Welding of Stainless Steel Sheets with a Gap. Applied Sciences 2021; 11: 2549. DOI: 10.3390/app11062549

22. Sun X, Cheng K. Multi-Scale Simulation of the Nano-Metric Cutting Process. International Journal of Advanced Manufacturing Technology 2010; 47: 891–901. DOI: 10.1007/s00170-009-2125-5

23. Perry TL, Werschmoeller D, Li X, et al. Pulsed Laser Polishing of Micro-Milled Ti6Al4V Samples. Journal of Manufacturing Processes 2009; 11: 74–81. DOI: 10.1016/j.jmapro.2009.10.001

24. Zhang C, Zhou J, Shen H. Role of Capillary and Thermocapillary Forces in Laser Polishing of Metals. Journal of Manufacturing Science and Engineering 2017; 139: 041019-1-041019–11. DOI: 10.1115/1.4035468

25. Li K, Zhao Z, Zhou H, et al. Numerical Analyses of Molten Pool Evolution in Laser Polishing Ti6Al4V. Journal of Manufacturing Processes 2020; 58: 574–584. DOI: 10.1016/j.jmapro.2020.08.045

26. Lee YS, Nordin M, Babu SS, et al. Influence of Fluid Convection on Weld Pool Formation in Laser Cladding. Welding Journal 2014; 93: 292s–300s. DOI: 10.1007/s11663-014-0054-7

27. Le T-N, Lo Y-L. Effects of Sulfur Concentration and Marangoni Convection on Melt-Pool Formation in Transition Mode of Selective Laser Melting Process. Materials & Design 2019; 179: 107866. DOI: 10.1016/j.matdes.2019.107866

28. Zhang Y, Zhang J. Modeling of Solidification Microstructure Evolution in Laser Powder Bed Fusion Fabricated 316L Stainless Steel Using Combined Computational Fluid Dynamics and Cellular Automata. Additive Manufacturing 2019; 28: 750–765. DOI: 10.1016/j.addma.2019.06.024

29. Tomashchuk I, Jouvard JM, Sallamand P, et al. Modeling of the Keyhole Asymmetry in Dissimilar Laser Welding. In: Comsol Conference Europe. 2020, pp. 14–16.

30. Faraji AH, Maletta C, Barbieri G, et al. Numerical Modeling of Fluid Flow, Heat, and Mass Transfer for Similar and Dissimilar Laser Welding of Ti-6Al-4V and Inconel 718. International Journal of Advanced Manufacturing Technology 2021; 114: 899–914. DOI: 10.1007/s00170-021-06868-z

31. Halim SB, Bannour S, Abderrazak K, et al. Numerical Analysis of Intermetallic Compounds Formed During Laser Welding of Aluminum-Magnesium Dissimilar Couple. Thermal Science and Engineering Progress 2021; 22: 100838. DOI: 10.1016/j.tsep.2020.100838

32. Sahu A, Bag S. Influence of Heat Input on Intermetallic Formation in Dissimilar Autogenous Laser Welding Between Inconel 718 and AISI 316L Steel. Proceedings of the Institution of Mechanical Engineers, Part B: Journal of Engineering Manufacture 2023; 237: 1422–1435. DOI: 10.1177/095440542211294

33. Chattopadhyay A, Muvvala G, Racherla V, et al. A Study on Laser Welding of Titanium and Stainless Steel. In: ASME 2018 13th International Manufacturing Science and Engineering Conference, MSEC 2018. 2018. DOI: 10.1115/MSEC2018-6584.

34. Zhou L, Li ZY, Song XG, et al. Influence of Laser Offset on Laser Welding-Brazing of Al/Brass Dissimilar Alloys. Journal of Alloys and Compounds 2017; 717: 78–92. DOI: 10.1016/j.jallcom.2017.05.099

35. Baqer YM, Ramesh S, Yusof F, et al. Challenges and Advances in Laser Welding of Dissimilar Light Alloys: Al/Mg, Al/Ti, and Mg/Ti Alloys. International journal of advanced manufacturing technology 2018; 95: 4353–4369. DOI: 10.1007/s00170-017-1565-6

36. Cui L, Wei Z, Ma B, et al. Microstructure Inhomogeneity of Dissimilar Steel/Al Butt Joints Produced by Laser Offset Welding. Journal of Manufacturing Processes 2020; 50: 561–572. DOI: 10.1016/j.jmapro.2020.01.011

37. Huang W, Cai W, Rinker TJ, et al. Effects of Laser Oscillation on Metal Mixing, Microstructure, and Mechanical Property of Aluminum–Copper Welds. International Journal of Machine Tools and Manufacture 2023; 188: 104020. DOI: 10.1016/j.ijmachtools.2023.104020

38. Borrmann S, Kratzsch C, Halbauer L, et al. Electron beam welding of CrMnNi-steels: CFD-modeling with temperature sensitive thermophysical properties. International Journal of Heat and Mass Transfer 2019; 139: 442–455. DOI: 10.1016/j.ijheatmasstransfer.2019.04.125

39. Shcherbakov AV, Gaponova DA, Sliva AP, et al. Multiphysic Simulation of Molten Pool Transients for Electron Beam Welding and Additive Manufacturing Processes Investigation. Journal of Physics: Conference Series; 1730. January 2021. DOI: 10.1088/1742-6596/1730/1/012027.

40. Shen H, Pan Y, Zhou J, et al. Forming Mechanism of Bump Shape in Pulsed Laser Melting of Stainless Steel. Journal of Heat Transfer; 139. Epub ahead of print 28 February 2017. DOI: 10.1115/1.4035710.

41. Hozoorbakhsh A, Hamdi M, Sarhan AADM, et al. CFD Modelling of Weld Pool Formation and Solidification in a Laser Micro-Welding Process. International Communications in Heat and Mass Transfer 2019; 101: 58–69. DOI: 10.1016/j.icheatmasstransfer.2019.01.001

42. Nikam SH, Quinn J, McFadden S. A Simplified Thermal Approximation Method to Include the Effects of Marangoni Convection in the Melt Pools of Processes That Involve Moving Point Heat Sources. 2021; 79: 537–552. DOI: 10.1080/10407782.2021.1872257

43. Kim CS. Thermophysical Properties of Stainless Steels. Argonne National Lab., Ill.(USA), 1975.

44. Zacharia T, David SA, Vitek JM, et al. Weld Pool Development During GTA and Laser Beam Welding of Type 304 Stainless Steel, Part I — Theoretical Analysis. Welding Journal 1989; 68: 499s–509s.

45. Vora HD, Santhanakrishnan S, Harimkar SP, et al. One-Dimensional Multipulse Laser Machining of Structural Alumina: Evolution of Surface Topography. International Journal of Advanced Manufacturing Technology 2013; 68: 69–83. DOI: 10.1007/s00170-012-4709-8

46. Dada M, Popoola P, Mathe N, et al. 2D Numerical Model for Heat Transfer on a Laser Deposited High Entropy Alloy Baseplate Using Comsol Multiphysics. Materials Today: Proceedings 2022; 50: 2541–2546. DOI: 10.1016/j.matpr.2021.12.068

47. Shah D, Volkov AN. Combined Smoothed Particle Hydrodynamics – Ray Tracing Method for Simulations of Keyhole Formation in Laser Melting of Bulk and Powder Metal Targets. In: ASME International Mechanical Engineering Congress and Exposition, Proceedings (IMECE). 2019. DOI: 10.1115/IMECE2019-11596.

48. Ansari P, Rehman AU, Pitir F, et al. Selective Laser Melting of 316L Austenitic Stainless Steel: Detailed Process Understanding Using Multiphysics Simulation and Experimentation. Metals (Basel) 2021; 11: 1076. DOI: 10.3390/met11071076

49. Indhu R, Vivek V, Sarathkumar L, et al. Overview of Laser Absorptivity Measurement Techniques for Material Processing. Lasers in Manufacturing and Materials Processing 2018; 5: 458–481. DOI: 10.1007/s40516-018-0075-1

50. Vadali M, Ma C, Duffie NA, et al. Effects of Pulse Duration on Laser Micro Polishing. Journal of Micro and Nano-Manufacturing; 1. Epub ahead of print 2013. DOI: 10.1115/1.4023756.

51. Li Z, Mukai K, Zeze M, et al. Determination of the Surface Tension of Liquid Stainless Steel. Journal of Materials Science 2005; 40: 2191–2195. DOI: 10.1007/s10853-005-1931-x

52. Bag S, De A. Computational Modelling of Conduction Mode Laser Welding Process. In: Laser Welding. Engineering Electrical and Electronic Engineering Sciyo. IntechOpen, pp. 133–160. DOI: 10.5772/9861

53. De Bono P, Allen C, D'Angelo G, et al. Investigation of Optical Sensor Approaches for Real-Time Monitoring During Fibre Laser Welding. Journal of Laser Applications; 29. 2017. DOI: 10.2351/1.4983253.

54. Huang W, Kovacevic R. Feasibility Study of Using Acoustic Signals for Online Monitoring of the Depth of Weld in the Laser Welding of High-Strength Steels. Proceedings of the Institution of Mechanical Engineers, Part B: Journal of Engineering Manufacture 2009; 223: 343–361. DOI: 10.1243/09544054JEM1320.